



LAWRENCE  
LIVERMORE  
NATIONAL  
LABORATORY

# Kinematic Finite-Source Model for the August 24, 2014 South Napa, CA Earthquake from Joint Inversion of Seismic, GPS and InSAR Data

D. S. Dreger, M. H. Huang, A. J. Rodgers, T.  
Taira, K. Wooddell

December 10, 2014

Seismological Research Letters

## **Disclaimer**

---

This document was prepared as an account of work sponsored by an agency of the United States government. Neither the United States government nor Lawrence Livermore National Security, LLC, nor any of their employees makes any warranty, expressed or implied, or assumes any legal liability or responsibility for the accuracy, completeness, or usefulness of any information, apparatus, product, or process disclosed, or represents that its use would not infringe privately owned rights. Reference herein to any specific commercial product, process, or service by trade name, trademark, manufacturer, or otherwise does not necessarily constitute or imply its endorsement, recommendation, or favoring by the United States government or Lawrence Livermore National Security, LLC. The views and opinions of authors expressed herein do not necessarily state or reflect those of the United States government or Lawrence Livermore National Security, LLC, and shall not be used for advertising or product endorsement purposes.

# Kinematic Finite-Source Model for the August 24, 2014 South Napa, CA Earthquake from Joint Inversion of Seismic, GPS and InSAR Data

Douglas S. Dreger<sup>1</sup>, Mong-Han Huang<sup>1</sup>, Arthur Rodgers<sup>2</sup>, Taka'aki Taira<sup>1</sup>, Kathryn Wooddell<sup>1</sup>

1. Berkeley Seismological Laboratory
2. Geophysical Monitoring Program, Lawrence Livermore National Laboratory, Livermore, CA 95441

## Supplemental Materials

This article has supplemental material with additional illustrations and a 3D wave propagation movie.

## Introduction

On August 24, 2014 at 10:20:44.06 UTC a large earthquake struck the north San Francisco Bay region, approximately 10 km SSW of Napa, California, causing local damage in older wood frame and masonry buildings, road surfaces, sidewalk and masonry wall structures (Bray et al., 2014). Using long-period (50 to 20 second) three-component, complete displacement records the Berkeley Seismological Laboratory (BSL) estimated the scalar seismic moment at  $1.32 \times 10^{18}$  Nm for a depth of 11 km, corresponding to a moment magnitude of Mw 6.0. The strike/dip/rake from the seismic moment tensor solution was found to be  $155^\circ/82^\circ/-172^\circ$ , which is in overall agreement with the trends of structures comprising the West Napa fault system (Figure 1). Geologic mapping revealed an approximately 14 km long surface rupture with maximum observed slip of 40-45 cm on a complex multi-branched fault system (Bray et al., 2014; EERI Special Earthquake Report, 2014; Oskin and Morelan, written communication, 2014). The largest surface offsets were found on a NW striking trend located approximately 1.8 km west of the mapped West Napa fault. Aftershocks are generally located west of

the western branch of the surface fault, which had the largest offsets, and indicates a westward dip of the primary fault plane (Figure 2).

An initial BSL kinematic finite-source model, based on three-component records from 8 Berkeley Digital Seismic Network Stations (BDSN) indicated unilateral, up-dip rupture to the NW reaching to within 2 km of the surface (Dreger, 2014). The slip centroid in that model was substantially shallower than the moment tensor result at approximately 6 km depth. The kinematic slip model indicated considerable directivity focusing of seismic energy toward the populated regions of Napa County, consistent with the level of recorded motions and damage in the region (Bray et al., 2014).

The earthquake was well recorded by the broadband BDSN network, and the strong motion stations operated by the California Geologic Survey and the US Geologic Survey, the Plate Boundary Observatory (PBO) continuous GPS network, and two radar interferometry scenes (ascending and descending orbits) from the COSMO-SkyMed satellite. In this paper we refine the kinematic finite-source model for the mainshock by combining the seismic waveform, GPS and InSAR geodetic data and use this model to investigate 3D wave propagation effects on the strong-motion wavefield.

## **Data Processing**

### *Seismic Waveform*

Given the time constraints for this manuscript we limited our analysis to the BDSN network. The 8 closest stations (Figure 1) provide good azimuthal coverage of the source. While our future work will fold in the strong motion data from other nearby strong motion sites, it should be noted that the BDSN stations are situated in well-constructed vaults at competent hard rock sites, and therefore have lesser site response concerns. Additionally, as will be shown later there are potentially complex 3D propagation effects within and adjacent to the Napa Valley that may complicate the use of the local data.

The acceleration records from the 8 BDSN sites (Figure 1), were mean offset and instrument corrected, integrated to displacement, and filtered with a two-pass bandpass Butterworth filter with corner frequencies of 0.02 to 1.0 Hz. The processed data was then resampled to 10 samples per second. Figure 3 shows the three-component displacement waveform data used in the inversion.

## *GPS*

We use the continuous GPS (cGPS) time series data from the *Plate Boundary Observatory* (PBO) network to calculate the coseismic displacement. All of the cGPS data are available on the USGS website (<http://earthquake.usgs.gov/monitoring/gps/SFBayArea/>). In this dataset, we use detrended daily solutions of the station position in the east-west, north-south, and up-down components. In general, the PBO cGPS daily solutions have ~1.8 mm uncertainty (Figure S1). Rapid postseismic displacement was observed at some sites and four alignment arrays were established indicating rapid postseismic displacement following coseismic offsets, however at many of the sites with the largest coseismic fault offsets, little postseismic displacement was observed (EERI Special Earthquake Report, 2014). Because of the presence of postseismic displacement, taking the differences of the GPS solutions one day before and after the earthquake is not reliable. To reduce the uncertainty in the estimate of the static offset and the postseismic displacement effect, we instead separately fit the GPS time series for 10 days prior and 10 days after the mainshock with least squares lines. The coseismic offset was then taken to be the difference of the two lines at the earthquake origin time (Figure S1). Figure 4 shows the horizontal static displacement vectors that we used in the inversion.

## *InSAR*

We use the COSMO-SkyMed (<http://www.cosmo-skymed.it>) ascending and descending interferograms that cover an approximately  $50 \times 80$  km<sup>2</sup> area surrounding the Napa earthquake to estimate the coseismic surface deformation. The COSMO-SkyMed is a right look (40° for ascending and 29° for descending orbit)

satellite and operates in X-Band (wavelength = 3.123 cm). The Napa coseismic interferograms are processed with ISCE interferometric processing system by the ARIA team at JPL-Caltech in collaboration with the Italian Space Agency (ASI) and the University of Basilicata. Figure 5 shows the coseismic displacement in ascending (June 19 – September 3, 2014) and descending (July 26 – August 27, 2014) tracks. The interferograms show the displacement projected from 3D to the line-of-sight (LOS), which is different in ascending or descending tracks. In addition, the interferograms contain part of the postseismic deformation that cannot be modeled by coseismic inversions since they were collected a few days after the Napa mainshock, although as will be shown there is not a large increase in seismic moment in the joint inversions compared to Seismic-Only inversions. We use the quadtree partitioning method (Jónsson et al., 2002) to down-sample the displacement fields. This method gives denser sampling in areas with larger and higher variation in deformation and reduces samples where the field is not dramatically changing with position. In this study we keep the total ascending and descending sampling to about 1,000 points total to smooth local variation and to better balance the number of observations with the two other data sets.

## **Inversion Setup**

The method used to simultaneously invert the seismic waveform, GPS and InSAR geodetic data is based on the method of Hartzell and Heaton (1983), as implemented in Kaverina et al. (2002) and Huang et al. (2013). This approach assumes a constant rupture velocity, and multiple time windows to account for some variation in rupture speed and the local rise time. In addition, it is possible to invert for variable slip direction. In this application we assumed a fixed rise time of 0.3 seconds and three time windows separated by 0.15 seconds. Since we have low-pass filtered the data at 1 Hz to remove higher frequency arrivals that can be strongly affected by lateral heterogeneity, we are not able to resolve variations in rise time. The inversion was also setup to solve for variations in rake between  $-135^\circ$  to  $-225^\circ$ .

The Green's functions for the seismic waveform part of the inversion were computed with a Fortran frequency wavenumber integration program, written by Chandan Saikia, based on the method of Wang & Herrmann (1980). For the geodetic part of the inversion, the static displacement Green's functions are computed using the programs EDGRN/EDCMP (Wang et al. 2003), which allows for the calculation of the Green's functions relating unit slip on each source subfault dislocation to surface displacements in a layered elastic model over a half-space. The same layered-elastic velocity structure GIL7 (e.g. Pasyanos et al., 1996), which was calibrated through broadband waveform modeling for the central coast region, and is routinely used by the BSL to compute seismic moment tensors, was used for both the seismic waveform and the geodetic Green's functions.

Preliminary modeling used the double-couple parameters from the BSL moment tensor solution and the Northern California Seismic System (NCSS) hypocenter position. This fault plane was found to reach the surface close to the mapped location of the West Napa fault, which is about 1.8 km east of the largest surface offsets (EERI Special Earthquake Report, 2014; Bray et al., 2014; Mike Oskin & Alex Morelan, written communication, 2014). There are minor surface offsets on the eastern strands of the fault, as indicated in the InSAR and UAVSAR data (e.g. Bray et al., 2014). This model was found to be inconsistent with the position of opposing motions in the InSAR LOS data, and we therefore adjusted the single-plane fault model used in the inversion to fit those observations, as well as the NCSS aftershock locations, and the surface slip (Figure 2b). This adjustment required a slight change in the strike and dip of the fault plane, and a 1.8 km shift of the fault model hypocenter to the west, as given in Table 1. The changes to the focal parameters are within the uncertainty of the BSL moment tensor solution.

**Table 1: Hypocenter Focal Parameters Used in Finite-Source Model**

Date and Origin Time	Latitude	Longitude	Depth (km)	Strike (°)	Dip (°)	Rake (°)
08/24/2014 10:22:44.06 UTC	38.2200	-122.3335	11.4	160	80	variable between -135 and -225

## Inversion Results

Assuming the hypocenter coordinates in Table 1, a three time-window, variable rake inversion was performed using the approach of Hartzell and Heaton (1983), as implemented by Kaverina et al., (2002). The maximum rupture velocity was found iteratively by performing inversions with different values and comparing a quantitative measure of fit based on a variance reduction as defined in equation 1.

$$VR = \left[ 1 - \frac{\sum_i (d_i - s_i)^2}{\sum_i d_i^2} \right] \times 100 \quad (1)$$

where  $d_i$  is the observed data and  $s_i$  its prediction based on the model.

Figure 2a shows the slip distribution recovered from simultaneous inversion of the seismic waveforms, GPS and InSAR data for a rupture velocity 2.9 km/s, corresponding to 85% of the shear wave velocity below 5 km depth in the GIL7 velocity model. As shown in Figure S2 the fit to the data was found to increase with increasing rupture velocity to a maximum near the shear wave velocity. The fit was observed to decrease for rupture velocity greater than the shear-wave velocity. We elected to present the model for 2.9 km/s since a rupture velocity of 85% of the shear wave velocity has been commonly observed. The slip model does not



dramatically change for values of rupture velocity from 80 to 90% of the shear wave velocity.

The more salient features of the kinematic model are the relatively fast rupture velocity, and the large, more or less continuous patch of slip extending from 0 to 13 km NW of the hypocenter in Figure 2a. The slip is also confined up-dip from the hypocenter at 11 km depth, extending to the surface. The average and peak slip are 0.21 and 1.15 m respectively. Aftershocks from the NCSS catalog tend to locate at the bottom edges of the main slip patch. The inversion allowed for variable rake between  $-135^{\circ}$  and  $-225^{\circ}$ , and for the most part, the slip is nearly pure right-lateral strike-slip, consistent with the moment tensor solution. At shallower depths, especially at the northern end of the slip model between -13 and -8 km on Figure 2a, there is an increased reverse component in the slip model. This change in slip angle greatly improves the fit to the GPS data, however considering the simple, single-plane model, and the fact that the surface offsets do change to a more northerly trajectory in this location (EERI Special Earthquake Report, 2014) it may be an artifact. This feature may suggest improvements in the source model in future work.

There is also a small amount of shallow slip 5 to 10 km southeast of the hypocenter (Figure 2a), which is present in all of the models (Figure S3). Through the course of the modeling this slip was found to be stable: it improves the fit to the large offset observed at PBO station P261 southeast of the fault and it is also present in the seismic-only model (Figure S3c). The InSAR observations (EERI Special Earthquake Report, 2014) do show minor offsets in this region on a fault located approximately 1 km to the east, where surface offsets were mapped (EERI Special Earthquake Report, 2014).

The three data sets were given equal weight in the inversion, and smoothing was adjusted to obtain the smoothest model that still retained a high level of fit to the data. The fit to the individual data sets using equation 1 is shown in Table 2.

Figures 3, 4 and 5 compare the fit to the seismic waveform, GPS and InSAR data, respectively. As Figure 3 shows, the waveform fits in the relatively low-frequency

(0.02 to 1.0 Hz) passband are good. There are some stations, notably BDM and BKS that fit poorly on the north-south components in which the extended surface wave train is not matched, and which could be due to 3D path effects since the paths to these stations cross the deep San Pablo bay (BKS) and the Sacramento River delta (BDM). On the other hand, the fits to the surface waves at stations MCCM and FARB are quite good. An exceptional fit to the GPS data (Figure 4) was obtained. The biggest misfit is for PBO station P264 located to the northeast of the main slip patch in which the model estimates only half of the observed southwestward deformation. In Figure 5, the InSAR observations provide good coverage around the source and the fits are good for both the ascending and descending tracks. The largest misfits are located several km northeast of the northern most surface slip in the Napa Valley. The large observed line-of-sight (LOS) changes there could partially be due to a hydrologic response to the earthquake as well as early rapid postseismic deformation (Bray et al., 2014), and possibly complexity in the fault geometry at the northern end of the rupture.

Figure S3 compares slip models for the preferred Seismic-GPS-InSAR case, and the Seismic-GPS and Seismic-Only cases. All of the models are similar, though the addition of the two geodetic datasets does increase the amount of shallow slip, which is more consistent with the observation of surface offsets. It is also notable that the scalar seismic moment increases with the inclusion of the geodetic datasets where the moment of the Seismic-GPS-InSAR case is approximately 14% larger than the Seismic-Only case indicating that there is a contribution from postseismic deformation. The BSL seismic moment tensor solution yielded a scalar moment of  $1.32 \times 10^{18}$  Nm (Mw 6.0), which is approximately 5% larger than the Seismic-Only finite-source result and lies between the Seismic-Only and the Seismic-GPS solution. The NCSS aftershocks locate in a “hole” in slip in the seismic waveform only model extending approximately 2-3 km updip and to the NW of the hypocenter (Figure S3). The inclusion of the geodetic data increases the slip in this region of the fault, possibly due to postseismic slip. Forward fitting of the InSAR and GPS data with the Seismic-Only model yielded goodness of fit values of 44.9% and 89.0% which are

fairly good, illustrating the consistency between the data sets, however the joint inversion significantly improved the fit to the geodetic data, and had only a minor detrimental effect on the fit to the seismic waveform data.

**Table 2: Summary of Inversion Fit and Scalar Moment**

Models	Fit (seis/gps/sar)	Moment (Nm)	Mw
Seismic-GPS-InSAR	62.1/94.9/69.0	$1.44 \times 10^{18}$	6.07
Seismic-GPS	66.7/94.9/na	$1.37 \times 10^{18}$	6.06
Seismic-Only	67.6/na/na	$1.26 \times 10^{18}$	6.03

### Three-Dimensional (3D) Ground Motion Simulations

The South Napa earthquake occurred in an area of complex geologic structure. Large ground motions and damage were likely related to contributions from source slip and directivity, path effects and site response. Details of sub-surface structure are represented in the USGS 3D geologic and seismic velocity model (USGS, 2014). The surface shear-wave speed and depth (relative to the surface topography) to the shear-wave speed of 1000 m/s (proxy for basin depth) in the near-source region is shown in Figure S4. These images indicate that deep (~1000 m) sedimentary structures are present adjacent to the West Napa Fault, with the Napa Valley to the north, Sonoma Valley to the west and the San Pablo Basin to the south. Low wave speed sedimentary basins in the Napa and Sonoma Valleys are separated by high

245 wave speed hard rock hills. Previous studies have found this model can predict  
246 observed waveforms for frequencies at or below 1 Hz reasonably well (Rodgers et  
247 al., 2008; Kim et al., 2010; Aagaard et al., 2010).

248 Ground motion simulations were performed using SW4, an anelastic finite  
249 difference code, which solves the displacement formulation using a summation-by-  
250 parts principle (Petersson and Sjogreen, 2013, 2014; CIG, 2014). Simulations used a  
251 minimum shear wave speed of 400 m/s and a grid spacing of 100 m, allowing  
252 accurate simulation of frequencies up to 0.5 Hz with 8 points per wavelength of the  
253 highest frequency.

254 In order to investigate the effects of inferred 3D structure we computed the ground  
255 motion for the plane-layered (1D) GIL7 model (e.g. Pasyanos et al., 1996) and the  
256 USGS 3D model. 3D simulations shown here included surface topography, though  
257 this has only a minor effect on the low-frequency ( $< 0.5$  Hz) motions. Figure 6  
258 shows the magnitude of the ground velocity response at 5 seconds after the rupture  
259 initiation for the 1D GIL7 and 3D USGS models. An animation comparing the 1D and  
260 3D response is included in the electronic supplement. The response for the 1D  
261 model shows the expected mostly symmetric response across the fault plane, with  
262 symmetry broken only by the non-vertical dip. Motions are slightly higher on the  
263 hanging wall (west). The simulated motions for the 3D model show a more complex  
264 response. The 3D case predicts reduced motions in the forward directivity due  
265 incoherence in the 3D response in the hills separating the Napa and Sonoma Valleys.  
266 The basin edges around the hills north of the fault delineate the stronger shaking  
267 and the shaking persists in the Napa Valley much longer than for the 1D case.  
268 Dramatic differences in the responses for 1D and 3D are seen south of the epicenter.  
269 For the 3D case shallow slip occurs just below or within the San Pablo Basin  
270 structure, which has a depth to the shear wave speed of 1000 m/s of 1200 m (Figure  
271 S4). The 3D simulation predicts ground motions in this area ( $\sim 30$ -40 cm/s), a little  
272 higher than was observed (20 cm/s in Vallejo). This simulation highlights the need  
273 to include 3D structure in source inversions, and to develop adjustments to the 3D  
274 velocity structure used for ground motion simulations.

275

## 276 **Discussion and Conclusions**

277 The model presented here is well constrained by all three data sets. The results  
278 show that the earthquake ruptured principally up-dip and toward the northwest.  
279 This likely had a significant directivity effect leading to the high level of strong  
280 ground motion observed in the Napa Valley and vicinity (Bray et al., 2014). An  
281 empirical Green's function approach, in which the seismic waveforms for a Mw 3.9  
282 aftershock were spectrally deconvolved from the mainshock records reveals a  
283 narrowing of the seismic moment rate functions to the NW (Figure S5) indicative of  
284 directivity in that direction.

285 The presented model was developed to align with the primary surface offset and the  
286 InSAR data. The location of where large surface offsets have been reported (Oskin  
287 and Morelan, written communication, 2014; Bray et al., 2014) is above the portion  
288 of the finite-source model with the large amplitude shallow slip. However the  
289 surface faulting and InSAR observations do suggest a more complicated fault  
290 structure (EERI Special Earthquake Report, 2014) than presented here. It remains  
291 an open question as to whether this surface complexity extends to depth. One  
292 possible model is that subsidiary faults branch upward from a primary steeply west-  
293 dipping fault that intersects the surface at the West Napa fault, creating a flower  
294 structure system of faults at the surface. It is presently unclear whether the seismic  
295 waveform and geodetic data sets would be capable of resolving such complexity,  
296 however future work should investigate this possibility.

297 The simulation of the seismic wavefield using the obtained kinematic finite-source  
298 model, and the USGS 3D velocity model (USGS, 2014) indicates that 3D  
299 heterogeneity in seismic velocity structure has a significant effect on the seismic  
300 wave propagation. In order to obtain better constraint on the seismic source future  
301 work will utilize source-receiver reciprocity and the USGS 3D velocity model to  
302 estimate Green's functions including 3D propagation effects due to lateral velocity  
303 changes, deep depositional basins, and the NW trending river valleys.

## Acknowledgements

We thank Jessica Murray and Ingrid Johansson for advice pertaining to GPS solutions. The interferograms used in this study are processed by JPL-Caltech, NASA. Waveform data were obtained from the Northern California Earthquake Data Center (NCEDC) with help from Dr. Douglas Neuhauser (NCEDC, 2014). Broadband waveforms were obtained from the Berkeley Digital Seismic Network and Northern Hayward Fault Network, operated by the Berkeley Seismological Laboratory, University of California, Berkeley. Strong motion data were obtained from the Northern California Seismic Network, operated by the U.S. Geological Survey, Menlo Park. We used the open-source SW4 anelastic finite difference code distributed by the Computational Infrastructure for Geodynamics (CIG, 2014). 3D ground motion simulations were performed on the Cab Linux cluster operated by Livermore Computing, Lawrence Livermore National Laboratory. This work was performed in part under the auspices of the U.S. Department of Energy by Lawrence Livermore National Laboratory under Contract DE-AC52-07NA27344.

## References

- Aagaard, B. T., R. W. Graves, A. J. Rodgers, T. M. Brocher, R. W. Simpson, D. Dreger, N. A. Petersson, S. C. Larsen, S. Ma and R. C. Jachens, Ground-Motion Modeling of Hayward Fault Scenario Earthquakes, Part II: Simulation of Long-Period and Broadband Ground Motions, *Bull. Seismol. Soc. Am.*, 100, 2945-2977, (2010), DOI: 10.1785/0120090379.
- Bray, J., J. Cohen-Waeber, T. Dawson, T. Kishida, and N. Sitar (2014). Geotechnical Engineering Reconnaissance of the August 24, 2014 M6 South Napa Earthquake, GEER Association Report, No. GEER-037, ver. 1., 402pp.
- Computational Infrastructure for Geodynamics, (2014). Website: <http://geodynamics.org/cig/software/sw4/>, accessed December 1, 2014.
- Dreger, D. S. (2014). Preliminary UC Berkeley Finite-Source Model for the August 24, 2014 Mw6.0 West Napa Earthquake, <http://seismo.berkeley.edu/napaquake>, last accessed Dec. 1, 2014.
- EERI Special Earthquake Report (2014). M 6.0 South Napa Earthquake of August 24, 2014, October 19, 2014, 21pp.

- Hartzell, S. H., and T. H. Heaton (1983), Inversion of strong ground motion and teleseismic waveform data for the fault rupture history of the 1979 Imperial Valley, California, earthquake, *Bull. Seism. Soc. Am.*, 73, 1553-1583.
- Huang, M-H, D. Dreger, R. Burgmann, S-H Yoo, and M. Hashimoto (2013). Joint inversion of seismic and geodetic data for the source of the 2010 March 4, Mw 6.3 Jia-Shian, SW Taiwan, earthquake, *Geophys. Journ. Int.*, doi:10.1093/gji/ggt058.
- Jónsson S., H. Zebker, P. Segall, and F. Amelung (2002). Fault slip distribution of the 1999 Mw 7.1 Hector Mine, California, Earthquake, estimated from satellite radar and GPS measurements. *Bull. Seismol. Soc. Am.*, **92**, 1377-1389.
- Kaverina, A., D. Dreger, and E. Price (2002) The combined inversion of seismic and geodetic data for the source process of the 16 October 1999 M (sub w) 7.1 Hector Mine, California, Earthquake, *Bull. Seism. Soc. Am.*, vol.92, no.4, pp.1266-1280.
- Kim, A., D. S. Dreger and S. Larsen (2010). Moderate Earthquake Ground-Motion Validation in the San Francisco Bay Area, *Bull. Seismol. Soc. Am.*, 100, 819-825.
- NCEDC (2014), Northern California Earthquake Data Center, UC Berkeley Seismological Laboratory. Dataset, doi:10.7932/NCEDC.
- Pasyanos, M. E., D. S. Dreger, and B. Romanowicz (1996), Towards Real-Time Determination of Regional Moment Tensors, *Bull. Seism. Soc. Am.*, 86, 1255-1269.
- Petersson, N. A. and B. Sjogreen (2013). User's guide to SW4, version 1.0, Lawrence Livermore National Laboratory technical report, LLNL-SM-642292.
- Petersson, N. A. and B. Sjogreen (2014) Super-grid modeling of the elastic wave equation in semi-bounded domains, *Comm. Comput. Phys.*, 16, 913-955.
- Rodgers, A., N. A. Petersson, S. Nilsson, B. Sjogreen, K. McCandless, Broadband waveform modeling of moderate earthquakes in the San Francisco Bay Area and preliminary assessment of the USGS 3D seismic velocity model, *Bull. Seismol. Soc. Am.*, 98, 969-988, (2008), DOI: 10.1785/0120060407.
- United States Geologic Survey (2014). 3D Geologic and Seismic Velocity Models of the San Francisco Bay Region, <http://earthquake.usgs.gov/data/3dgeologic/>, (website) accessed December 1, 2014.
- Wang, C.Y. & Herrmann, R.B., 1980. A numerical study of P-, SV-, and SH-wave generation in a plane layered medium, *Bull. seism. Soc. Am.*, 70(4), 1015-1036.
- Wang, R., Martin, F. & Roth, F., 2003. Computation of deformation induced by

381 earthquakes in multi-layered elastic crust: FORTRAN programs EDGRN/EDCMP,  
382 Comput. Geosci., 29, 195–207.  
383  
384



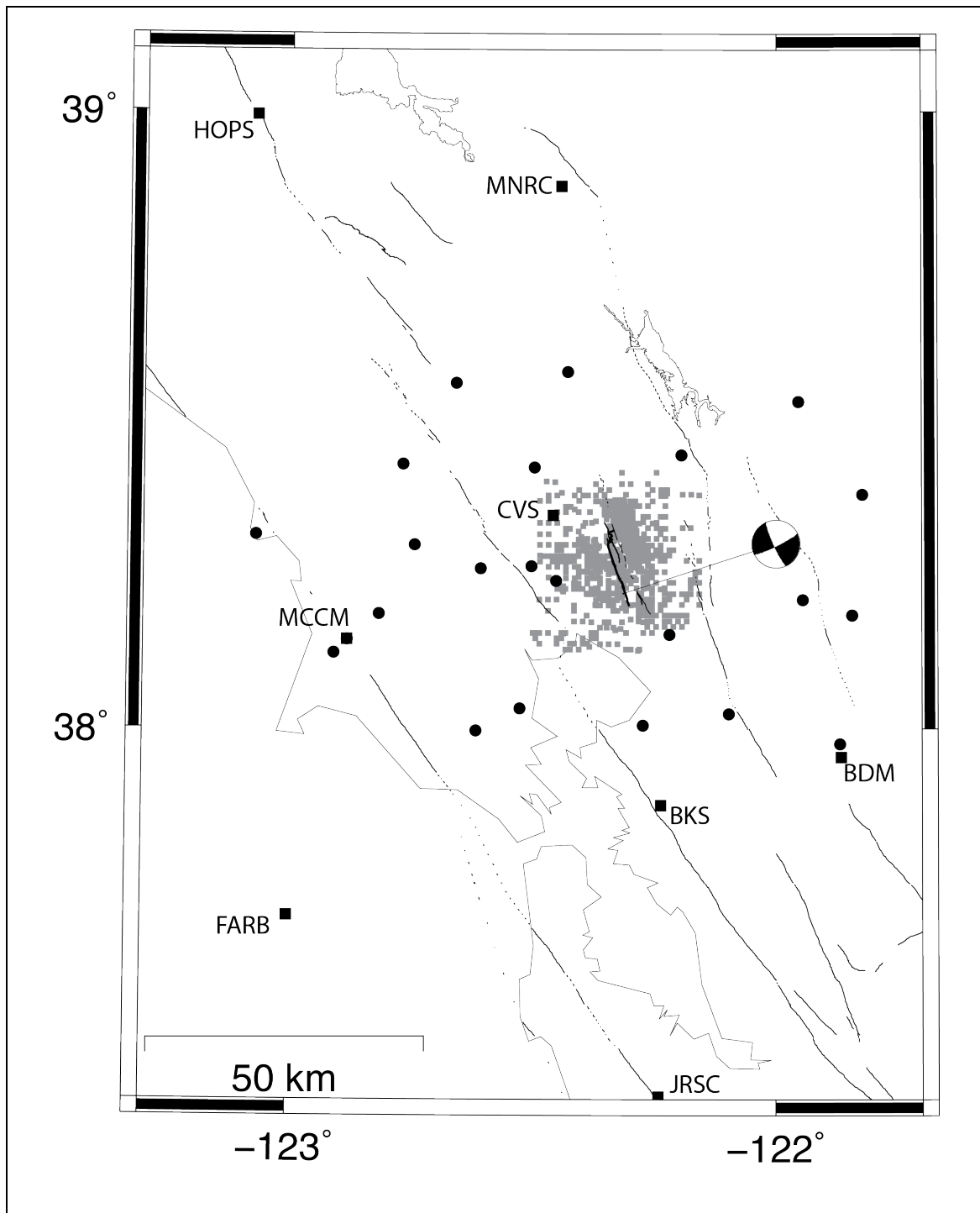
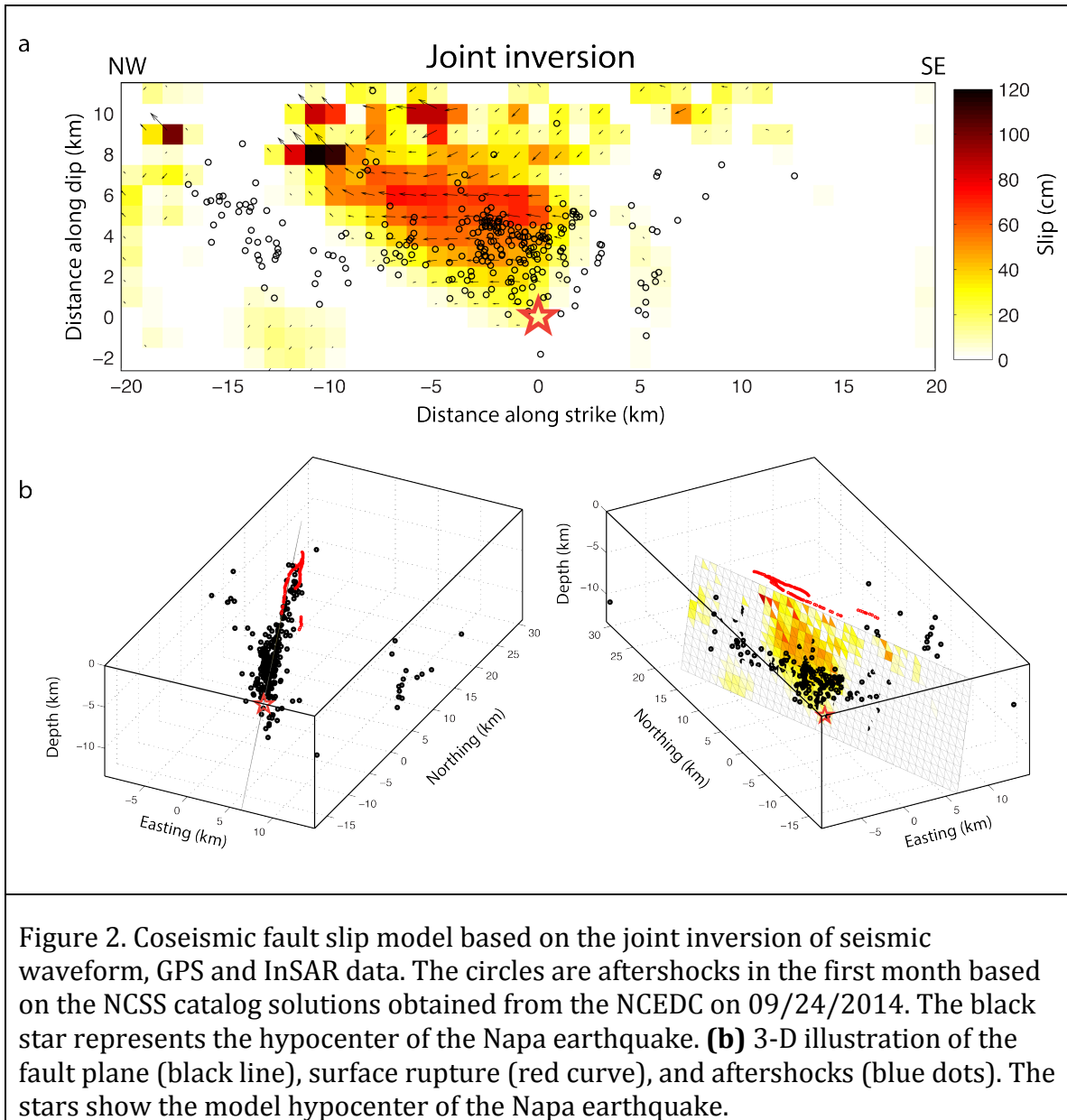
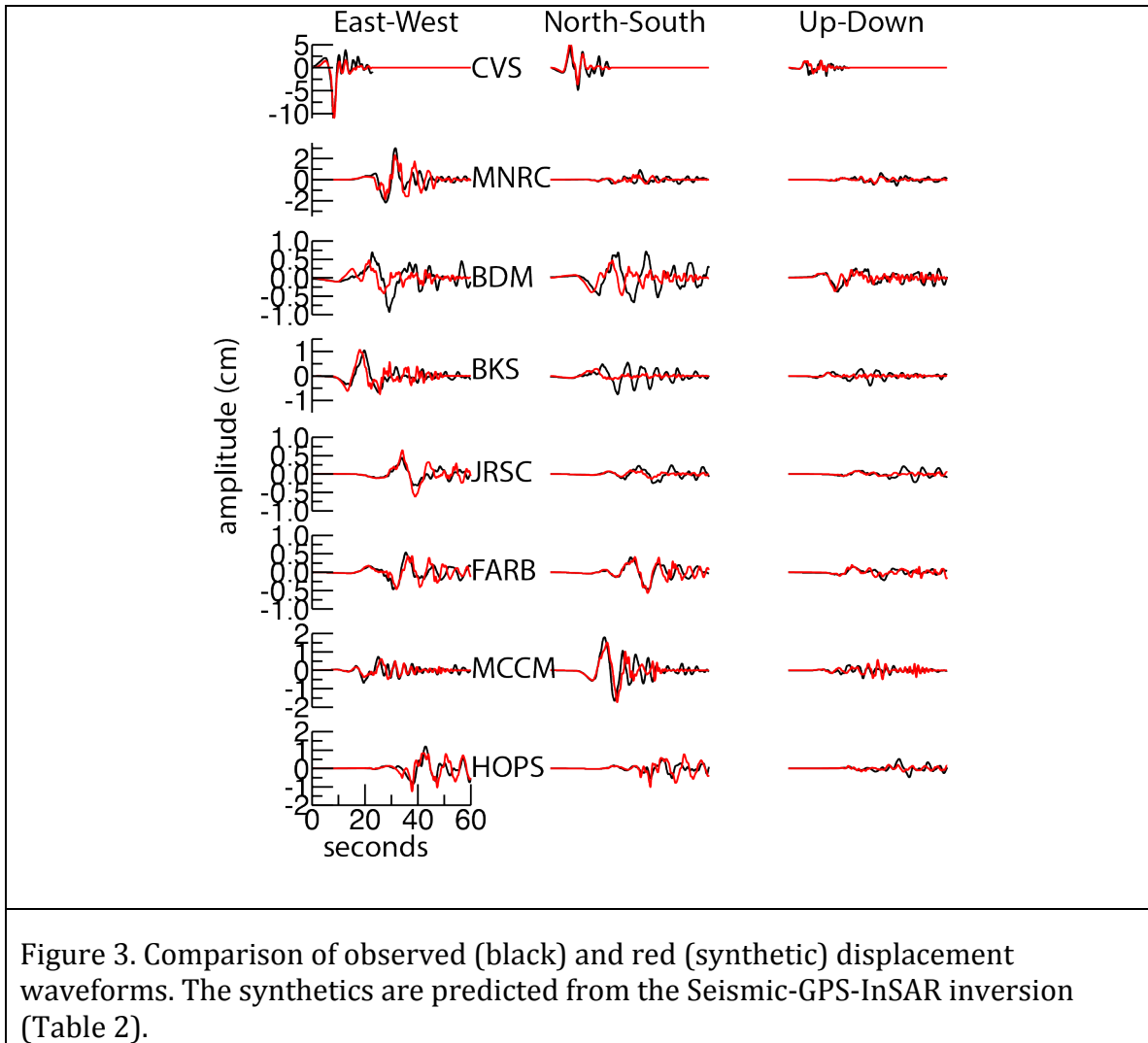


Figure 1. Locations of BDSN seismic stations are shown as squares and are labeled. PBO GPS sites are shown as circles, and the positions of InSAR returns are small grey squares. The Berkeley Seismological Laboratory focal mechanism is shown, and the thick line shows the mapped surface trace (EERI Special Earthquake Report, 2014).





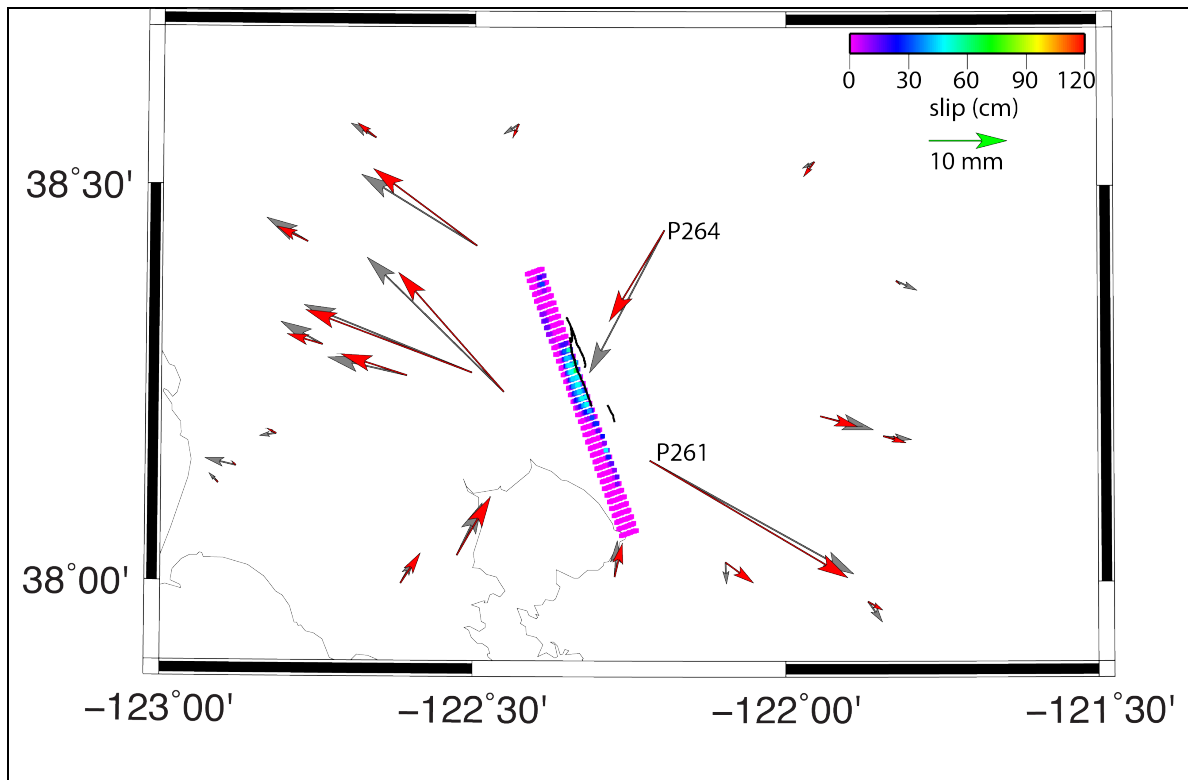


Figure 4. Map showing observed (grey) and synthetic (red) horizontal GPS vectors. The scale is given by the green arrow. The synthetics are based on the joint Seismic-GPS-InSAR inversion. The purple-to-blue colors are the coseismic fault slip (figure 2a) projected onto the surface.

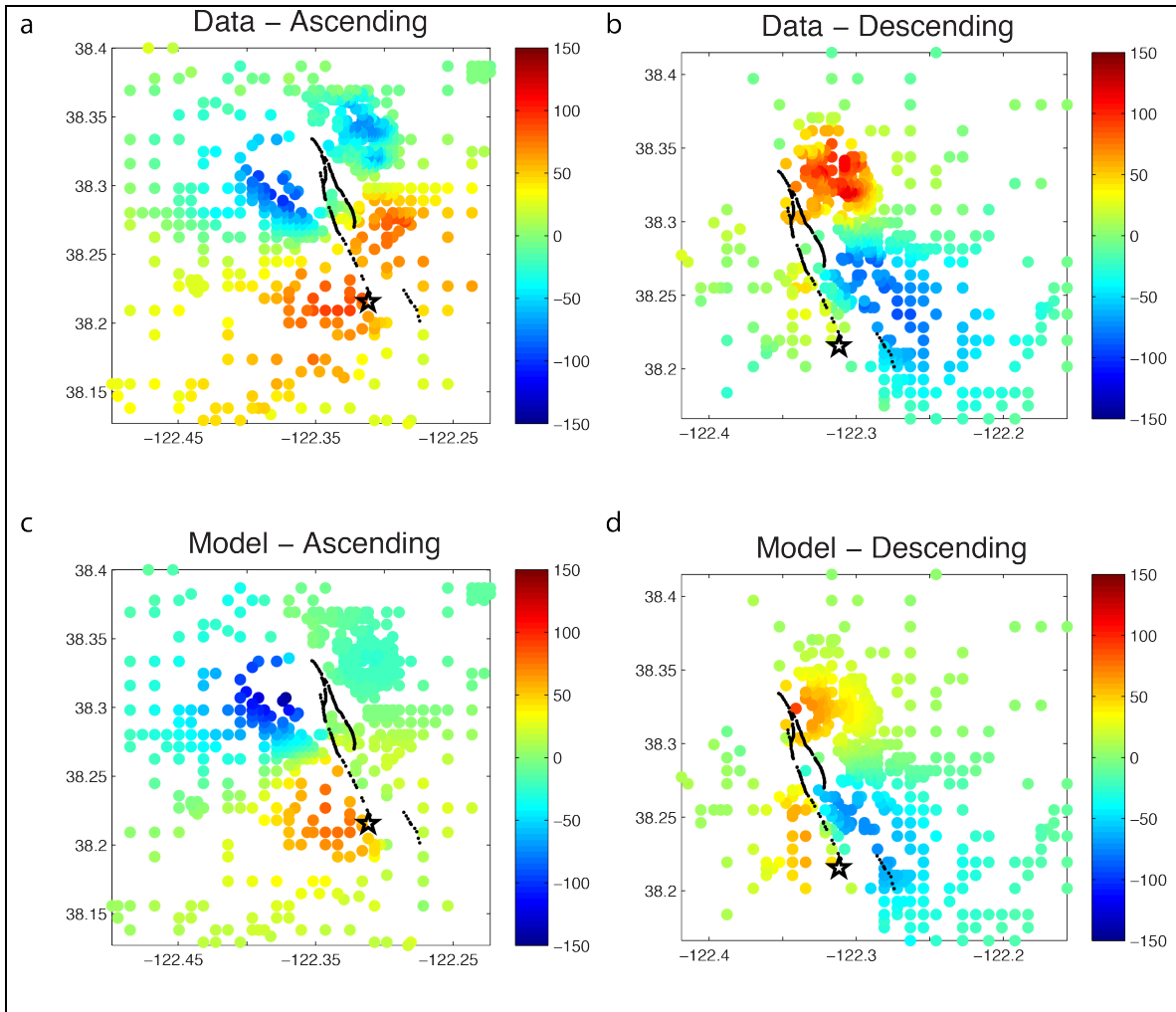
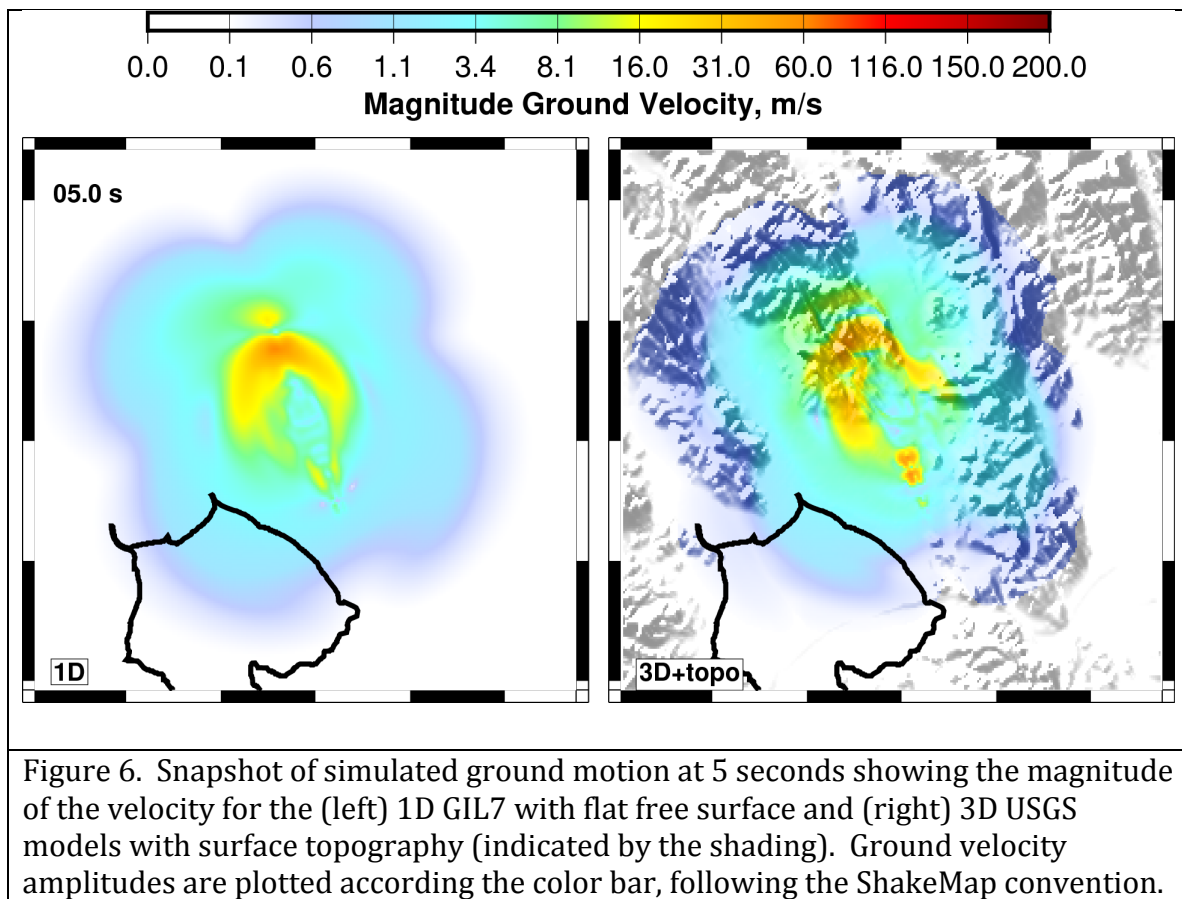


Figure 5. COSMO-SkyMed coseismic interferograms in **(a)** ascending (June 19 – September 3, 2014) and **(b)** descending (July 26 – August 27, 2014) orbits. The colored dots are InSAR measurements after downsampling using the quad-tree method (*Jónsson et al., 2002*). In **(a)**, the warmer colors represent uplift or westward displacement; the cooler colors represent subsidence or eastward displacement. In **(b)**, the warmer colors represent subsidence or eastward displacements; the cooler colors represent uplift or westward displacements. **(c)** and **(d)** are model predictions for the ascending and descending orbits, respectively. In each plot, the black star is the earthquake epicenter, and the black curve is the surface rupture.



394